



## RESEARCH ARTICLE

10.1002/2015WR017658

## Steady nonuniform shallow flow within emergent vegetation

Wei-Jie Wang<sup>1,2</sup>, Wen-Xin Huai<sup>1</sup>, Sally Thompson<sup>3</sup>, and Gabriel G. Katul<sup>2,4</sup>

## Key Points:

- Saint-Venant equation subject to a Manning-type roughness predicts water profile in vegetative flow
- The drag coefficient in steady nonuniform flow exhibits a parabolic shape along vegetation path
- Flow nonuniformity contributes to the parabolic feature

## Correspondence to:

W.-X. Huai,  
wxhuai@whu.edu.cn

## Citation:

Wang, W.-J., W.-X. Huai, S. Thompson, and G. G. Katul (2015), Steady nonuniform shallow flow within emergent vegetation, *Water Resour. Res.*, 51, 10047–10064, doi:10.1002/2015WR017658.

Received 4 JUN 2015

Accepted 1 DEC 2015

Accepted article online 7 DEC 2015

Published online 31 DEC 2015

<sup>1</sup>State Key Laboratory of Water Resources and Hydropower Engineering Science, Wuhan University, Wuhan, China, <sup>2</sup>Nicholas School of the Environment, Duke University, Durham, North Carolina, USA, <sup>3</sup>Department of Civil and Environmental Engineering, University of California at Berkeley, Berkeley, California, USA, <sup>4</sup>Department of Civil and Environmental Engineering, Duke University, Durham, North Carolina, USA

**Abstract** Surface flow redistribution on flat ground from crusted bare soil to vegetated patches following intense rainfall events elevates plant available water above that provided by rainfall. The significance of this surface water redistribution to sustaining vegetation in arid and semiarid regions is undisputed. What is disputed is the quantity and spatial distribution of the redistributed water. In ecohydrological models, such nonuniform flows are described using the Saint-Venant equation (SVE) subject to a Manning roughness coefficient closure. To explore these assumptions in the most idealized setting, flume experiments were conducted using rigid cylinders representing rigid vegetation with varying density. Flow was induced along the streamwise  $x$  direction by adjusting the free water surface height  $H(x)$  between the upstream and downstream boundaries mimicking the nonuniformity encountered in nature. In natural settings, such  $H(x)$  variations arise due to contrasts in infiltration capacity and ponded depths during storms. The measured  $H(x)$  values in the flume were interpreted using the SVE augmented with progressively elaborate approximations to the roughness representation. The simplest approximation employs a friction factor derived from a drag coefficient ( $C_d$ ) for isolated cylinders in a locally (but not globally) uniform flow and upscaled using the rod density that was varied across experiments. Comparison between measured and modeled  $H(x)$  suggested that such a “naive” approach overpredicts  $H(x)$ . Blockage was then incorporated into the SVE model calculations but resulted in underestimation of  $H(x)$ . Biases in modeled  $H(x)$  suggest that  $C_d$  must be varying in  $x$  beyond what a local or bulk Reynolds number predicts. Inferred  $C_d(x)$  from the flume experiments exhibited a near-parabolic shape most peaked in the densest canopy cases. The outcome of such  $C_d(x)$  variations is then summarized in a bulk resistance formulation that may be beneficial to modeling runoff processes on shallow slopes using SVE.

## 1. Introduction

In regions where the landscape is a two-phase mosaic comprising of bare soil and vegetation, lateral water redistribution following intense rainfall events appears to be necessary for sustaining vegetation biomass (grassy, shrubby, or combination). On flat or gently sloping terrain, differential free water surface elevations can arise between bare soil locations and vegetated patches during intense rainfall events because of contrasts in infiltration capacity that can span several orders of magnitude [Bromley *et al.*, 1997; Valentin and d’Herbès, 1999; Thompson *et al.*, 2010; Assouline *et al.*, 2015]. These differences in the free water surface can drive flow between bare and vegetated sites, which upon infiltrating beneath vegetation canopies increases plant available water beyond that provided directly by throughfall. A large corpus of data and model results suggest that the aforementioned lateral surface water redistribution is an essential mechanism for vegetation maintenance in arid and semiarid regions [Rietkerk *et al.*, 2002; Thompson *et al.*, 2008; Kefi *et al.*, 2008; Kletter *et al.*, 2009; Chen *et al.*, 2013; Assouline *et al.*, 2015]. These runoff-runon mechanisms are also thought to be integral to the formation of coherent spatial patterning of vegetation in some ecosystems systems [Rietkerk *et al.*, 2002], as illustrated in Figure 1, which shows a site in central Australia where a tenfold contrast in infiltration capacity was measured between bare and vegetated locations [Dunkerley, 2002].

Providing quantitative predictions about how the properties of the land surface, vegetation patch size and structure interact to determine the spatial distribution and total volume of infiltrated water in runoff situations remains challenging. Generally, the flows relevant to water redistribution occur on fairly flat slopes ( $\leq 2\%$ ) [Rietkerk *et al.*, 2002] that preclude formation of rills and flow concentration that can route

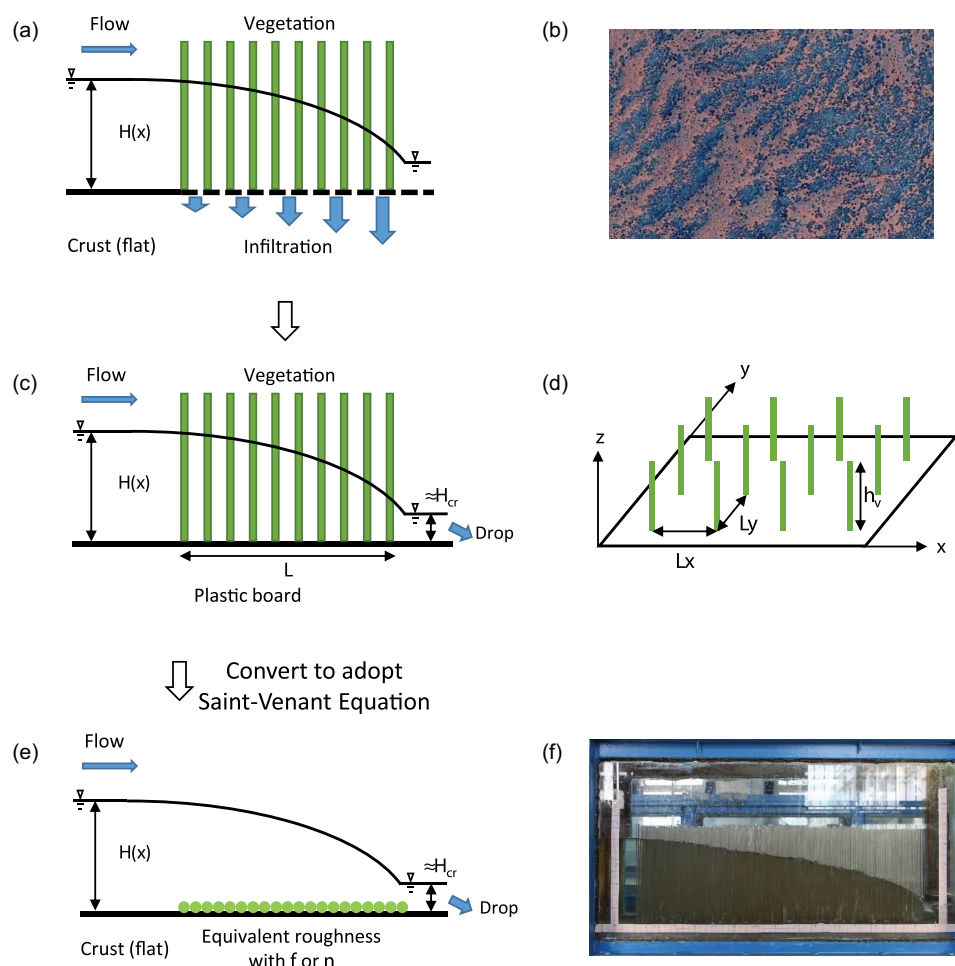


**Figure 1.** (a) Schematic of the flow from a crusted bare soil to a vegetated patch driven by infiltration contrast between the vegetation zone and the crusted (or nearly sealed) soil. (b) The occurrence of such lateral subsidence in arid and semiarid ecosystem showcased in Australia ( $-23.452226, 133.381763$ ) from Google Earth. (c) Modeling nonuniform vegetated flow in a laboratory experiment with a flow drop at the end of the vegetated section controlling the nonuniformity instead of a continuous infiltration process within the vegetated zone. (d) Arrangement of the cylinders in the flume experiments. (e) Prediction of the flow surface line  $H(x)$  from the Saint-Venant equation (SVE) where the drag force imposed by the vegetation on the flow is replaced by a bed and a side friction through an equivalent surface roughness linked to the vegetation drag coefficient  $C_d$  and the vegetation density. Translating the interaction of cylinders into an equivalent surface roughness to be used in modeling water subsidies using the SVE frames the scope of the work here. (f) An image taken by a side-view camera for Run A described in the experiments.

water around vegetated patches and decrease the efficiency of runoff as a mechanism directing water to vegetated patches. Thus, the spatial gradient of the free water surface tends to be the dominant factor driving water movement toward vegetated patches instead of the land-surface slope (Figure 1). Within vegetated patches, emergent vegetation imposes additional drag on the flowing water, causing it to decelerate (e.g., Figure 1). This mechanism increases the residence time of water within the vegetated patch and enhances the cumulative infiltration into the rooting zone [Rietkerk *et al.*, 2002; Thompson *et al.*, 2011; Konings *et al.*, 2011; Assouline *et al.*, 2015]. When integrated on seasonal to annual time scales, this water subsidy promotes further biomass growth and thus increases the residence time for water within the patch, generating a positive feedback on vegetation growth.

Quantitative predictions about the volume and spatial distribution of infiltrated water require a description of the lateral flow process. As outlined above, free surface gradients represent the major driving force for the flow on flat surfaces, meaning that kinematic representations widely used in runoff modeling [Smith *et al.*, 1995] are not applicable. On the other hand, the shallow ( $<5$  cm) flow depths expected and the uncertainties in the distribution of roughness elements imposed by the emergent vegetation preclude an explicit description of turbulent flow statistics in this zone. The key hydrological variables required for

quantifying the redistribution of water in Figure 1 are primarily bulk velocity (affecting the residence time) and water depth (affecting the infiltration rate). Depth and bulk velocity are natural outcomes of the Saint-Venant equation (SVE), subject to a suitable closure model to generate a friction factor,  $f$ , describing the effects of drag imposed by the vegetation on the flow. The SVE thus provides a suitable framework for modeling the movement of water from bare to vegetated sites [Abrahams *et al.*, 1986; Ajayi *et al.*, 2008; Holden *et al.*, 2008; Thompson *et al.*, 2011; Konings *et al.*, 2011; Kim *et al.*, 2012; Foti and Ramírez, 2013; Chen *et al.*, 2013; Assouline *et al.*, 2015]. In open channel settings, similar approaches have proven reasonably robust and generalizable [Green, 2005]. For example, individual plant species with differing spatial distributions of leaf area and stems have been shown to not significantly alter  $f$  [Nikora *et al.*, 2008]. Indeed, there is an extensive literature in “ecohydraulics” that addresses the effect of vegetation on the bulk flow, mean velocity, and the vertical distribution of turbulent stresses in uniform open channel flow subjected to various driving gradients [Järvelä, 2002; Poggi *et al.*, 2004a; Carollo *et al.*, 2005; Huthoff *et al.*, 2007; Nepf and Ghisalberti, 2008; Poggi *et al.*, 2009; Huai *et al.*, 2009; Luhar *et al.*, 2008; Katul *et al.*, 2011; Nepf, 2012; Konings *et al.*, 2012; Siniscalchi *et al.*, 2012; Huai *et al.*, 2013; Okamoto and Nezu, 2013; Huai *et al.*, 2014; Wang *et al.*, 2015; Banerjee *et al.*, 2015]. The specific case here, however, with emergent vegetation interacting with a nonuniform and complex flow in the absence of a strong driving land surface gradient, has yet to be explored. Furthermore, predictions from the SVE that are used in modeling water flow in such system have not been evaluated. The flume experiments described here aim to represent the main features of the free-surface-driven overland flow problem for flat, vegetated surfaces, and provide a basis for comparison with the predictions of the SVE. By no means these experiments are intended to describe all aspects and nuisances of the real system. However, they do provide some bench mark data to compare SVE calculations when closed with a prespecified local roughness or friction factor as commonly conducted in recent studies [Assouline *et al.*, 2015].

The flume experiments consisted of a flat surface with a short “vegetated” patch, composed of uniformly distributed cylinders, as shown in Figure 1. Flow at the upstream end is maintained as a fixed head condition (analogous to the ponded depth on a bare soil in the natural setting), and flow at the downstream end was held at a fixed (and lower) depth by adjusting the outflow conditions and the vegetation patch length. This is analogous to a situation where the infiltration rate increases with distance into the vegetated patch, rather than at the immediate interface between the vegetated and bare sites, a situation that occurs in banded vegetation communities within the Sahel [Galle *et al.*, 1999]. These head and flow boundary conditions were selected given the difficulty in adjusting a spatially variable infiltration rate contrast for different vegetation densities. All experiments were conducted using a steady flow rate  $Q$  that was selected to maintain an emergent vegetation state and subcritical depth. To facilitate comparisons with other experiments, vegetation stems were represented with rigid cylinders of diameter  $D$  anchored to the ground with  $L_x$  and  $L_y$  denoting longitudinal ( $x$ ) and transverse ( $y$ ) spacing distances between two adjacent cylinders as shown in Figure 1. The vegetation patch size and density were systematically varied to produce different flow conditions, and the steady, but nonuniform, water surface levels that resulted were imaged for each configuration (e.g., see Figure 1).

The flume experiments do not allow analysis of several features that could impact the runoff-runoff problem in practice, including nonuniformity in the vegetation distribution, wind and rain effects at the water surface, and microtopographic variations of the bed surface. Several other features of the general problem of describing flow over rough surfaces are also omitted in the analysis, primarily because they are unlikely to be significant for the runoff-runoff scenario in drylands. These include the relative submergence of the vegetation [Lawrence, 2000; Roche *et al.*, 2007; Poggi *et al.*, 2009], which will influence vegetation drag if the plant has a nonuniform distribution of biomass vertically, and the potential for bending or waving when the vegetation is flexible thereby allowing some reconfiguration and drag reduction [Velasco *et al.*, 2008; Kubrak *et al.*, 2008; Yang and Choi, 2009; Dijkstra and Uittenbogaard, 2010]. The slender and rigid canopy elements modeled in the flume here most closely resemble rigid desert grasses—a broad and extensive vegetation morphology in drylands (e.g., *Hilaria rigida* (USA) [Nobel, 1980], *Stipagrostis sabulicola* (Namibia) [Roth-Nebelsick *et al.*, 2012], and *Triodia* and *Plectrachne* genera (Australia) [Wasson and Nanninga, 1986]). The cylinders are also of uniform width thereby ignoring nonuniformity expected in stem size distribution. Finally, the experiments were narrowly focused on steady nonuniform flow. While the effects of nonsteadiness may be significant, they can be accommodated within the SVE framework described here provided

the nonuniformity in water depth maintains its gradual state [Woolhiser and Liggett, 1967; Thompson et al., 2011; Konings et al., 2011].

For each combination of vegetation patch size and density, the SVE was used to analyze the water surface levels that were imaged at steady state. The analysis considered several elaborations of the representation of the drag force induced by the vegetation. To relate the vegetation characteristics to a drag coefficient, the vegetation-induced drag force was conceptualized as an equivalent shear stress applied to the channel bed. The solution method involves identifying the roughness distribution (i.e., drag coefficient distribution) that yields the observed water surface profile for a specified  $Q$  (see Figure 1). For an isolated cylinder, that drag coefficient distribution can be depth integrated to yield a friction factor (or roughness value) that decreases monotonically with increasing Reynolds number in steady and uniform flow [Tanino and Nepf, 2008; Cheng and Nguyen, 2010].

Here the drag coefficients obtained from several published rigid rod-canopy studies were first considered. These drag coefficients were depth integrated and applied to the nonuniform flow experiments here after linking the drag coefficient to the friction factor. Their ability to reproduce the measured water level variation within the vegetated section at a given  $Q$  and vegetation density was explored within the SVE. As shown, unacceptable deviations between predicted and measured water levels were found, motivating an analysis of the spatial variation of the friction factor or roughness coefficient along the vegetated section for various vegetation densities but the same  $Q$ . A main outcome of this work is a bulk resistance formulation that summarizes the flume experiments and a bulk drag coefficient that may be operationally implemented in closure schemes for the SVE when predicting the lateral redistribution of water while accounting for nonuniformity in the flow, as shown in Figure 1.

## 2. Theory

### 2.1. Overview and Basic Definitions

Consider a rectangular channel with a constant width  $B$ , water depth  $H(x)$ , cross-sectional area  $A(x) = BH(x)$ , and hydraulic radius  $R(x) = A(x)/(B + 2H(x))$ . The flow in the channel occurs at a constant flow rate  $Q$  in streamwise direction  $x$ . The bulk velocity is  $U(x) = Q/A(x)$  (this definition is revised later to account for the vegetation volume within the channel). The friction slope  $S_f$  (or energy grade line slope) is defined as the total energy head loss per unit streamwise length:

$$S_f = -\frac{\partial E}{\partial x} = -\frac{\partial}{\partial x} \left( z_g + \frac{p}{\gamma} + \alpha_v \frac{U^2}{2g} \right), \quad (1)$$

where  $E$  is the total energy head,  $z_g$  is the elevation of channel ground above a datum,  $p = \gamma H$  is the hydrostatic pressure with  $\gamma = \rho g$  being the specific weight of the fluid,  $\alpha_v$  is a correction coefficient for the kinetic energy head ( $\alpha_v = 1$  is adopted here for simplicity given the shallow nature of the flow though it may vary with distance for nonuniform flow), and  $g$  is the gravitational acceleration. With bed slope  $S_0 = -\partial z_g / \partial x$ , equation (1) is rearranged in its familiar SVE form for steady conditions:

$$U \frac{\partial U}{\partial x} + g \frac{\partial H}{\partial x} - g(S_0 - S_f) = 0, \quad (2)$$

with bed slope  $S_0 \approx 0$  for the runoff problem that is considered here. Because  $S_f$  is finite and  $S_0 \approx 0$ , the kinematic wave approximation cannot be invoked. Also, with the advective term being significant and nonuniform along  $x$ , diffusive wave approximations also cannot be invoked. When combined with the continuity equation  $U(x) = Q/(BH(x))^{-1}$ , the SVE provides a second equation relating  $H$  and  $U$  while introducing a new variable  $S_f$  that is generally unknown and requires a mathematical closure to estimate its value from the channel flow variables ( $U$  and  $H$ ) and vegetation properties. A widely accepted relation used as a closure model is to assume locally uniform flow, which permits the use of Mannings equation (in SI units) to relate  $S_f$  to  $U$  and  $H$  using:

$$U = \frac{1}{n} R^{2/3} S_f^{1/2}, \quad (3)$$

provided the Manning roughness coefficient  $n$  is a priori known at this location [Thompson et al., 2011; Konings et al., 2011; Foti and Ramírez, 2013; Chen et al., 2013]. This assumption may be reasonable if the

overall change in water level across the entire vegetated patch length in Figure 1 is small or the nonuniformity in  $H(x)$  is gradual as is the case here. The  $S_f$  can also be calculated using the more common Darcy-Weisbach friction factor:

$$f = \frac{8gRS_f}{U^2}. \quad (4)$$

When combining equation (3) with equation (4), the two standard roughness parameters  $n$  and  $f$  are related using

$$n = \left( \frac{f}{8g} \right)^{1/2} R^{1/6}. \quad (5)$$

Hence, specifying  $n$  is equivalent to specifying  $f$ . For open channel flow without vegetation, the roughness parameter  $n$  (or  $f$ ) may be estimated from the mean protrusion height of the material covering the channel ground and sidewalls. However, such roughness determination becomes complicated in the presence of vegetation elements (stems or leaves). Steady and locally uniform flow conditions require a local force balance between the flow driving mechanism and the drag term. For a given length-scale  $dx$  along the streamwise direction, the flow driving mechanism is  $[\gamma BHdx(1-\phi_{veg})S_f]$  where  $\phi_{veg}$  is defined as the area concentration of stems, and the resistance forces are due to three terms: (1) vegetation drag  $[Bdx F_D]$ , with  $F_D$  the vegetation drag force per unit ground-area, (2) ground friction  $[Bdx(1-\phi_{veg})\tau_{ground}]$ , with  $\tau_{ground}$  the ground friction per unit ground-area, and (3) sidewall friction  $[2Hdx\tau_{wall}]$ , with  $\tau_{wall}$  the sidewall friction per unit sidewall area. The force balance between the driving mechanism and resistance along the streamwise direction yields

$$\gamma BHdx(1-\phi_{veg})S_f = Bdx F_D + Bdx(1-\phi_{veg})\tau_{ground} + 2Hdx\tau_{wall}, \quad (6)$$

that reduces to

$$\gamma BH(1-\phi_{veg})S_f = BF_D + B(1-\phi_{veg})\tau_{ground} + 2H\tau_{wall}, \quad (7)$$

where  $\tau_{ground} = (1/8)\rho U^2 f_{ground}$  and  $\tau_{wall} = (1/8)\rho U^2 f_{wall}$  given by Darcy-Weisbach formula with roughness parameter  $f_{ground}$  and  $f_{wall}$ . It is to be noted that on the right-hand side of equation (7), the vegetation drag  $BF_D$  is much larger than the ground and sidewall frictions  $B(1-\phi_{veg})\tau_{ground}$  and  $2H\tau_{wall}$ , and a discussion on the impact of boundary (ground and sidewall) friction is presented in a later section. Without the effect of ground and sidewalls, the simplified force balance yields

$$\gamma H(1-\phi_{veg})S_f = F_D. \quad (8)$$

For stems approximated by cylinders with diameter  $D$ , the spatially averaged vegetation drag per unit ground area is given by [Ghisalberti and Nepf, 2004; Nepf, 2012; Huai et al., 2014]

$$F_D = \frac{1}{2} C_d m D H \rho U^2, \quad (9)$$

where  $C_d$  is the depth-averaged drag coefficient of the cylindrical vegetation, and  $m = 1/(LxLy)$  is the number of vegetation stems per unit ground area. The  $D$  is interpreted as the frontal width of the vegetation stem (equivalent to the diameter of cylindrical vegetation elements). So the relationship between  $m$  and  $\phi_{veg}$  is  $\phi_{veg} = m\pi D^2/4$ . The sought-after slope  $S_f$  in the SVE can be linked to  $C_d$  by inserting the definition of the vegetation drag (equation (9)) into the force balance expression (equation (8)), yielding:

$$S_f = \frac{C_d m D}{(1-\phi_{veg})} \frac{U^2}{2g}. \quad (10)$$

Without the effect of sidewalls, the “effective” wetted length is the channel width  $B$  when adopting the concept of equivalent roughness imposed on ground from vegetation stems. The hydraulic radius can be calculated by  $R \approx HB/(B) = H$ , and an equivalent Darcy-Weisbach friction factor for the vegetation  $f = f_{veg}$  can now be derived by inserting equation (10) into equation (4) [Poggi et al., 2009].

$$f_{veg} = \frac{4C_d m D H}{1-\phi_{veg}}. \quad (11)$$



If  $C_d$  for the vegetated flow is known, then inserting equation (10) into SVE (equation (2)) allows the determination of  $H(x)$  provided an appropriate boundary condition (e.g.,  $H_0$  at  $x = 0$ ) is specified. It should be noted that the “effective flow width” is actually narrower than the channel width due to the presence of cylinders. To adjust for such narrowing effect, the effective flow width  $B_e$  is used instead of channel width  $B$  when solving the SVE. For a unit length along the streamwise direction, the bed area is  $B$  and the area occupied by water is  $B(1 - \phi_{veg})$ . Hence, the “effective flow width” is  $B_e = B(1 - \phi_{veg})$ . The bulk flow velocity within an emergent vegetated system can be determined as follows [Tanino and Nepf, 2008; Cheng and Nguyen, 2010]:

$$U(x) = \frac{Q}{B_e H(x)} = \frac{Q}{B(1 - \phi_{veg}) H(x)}. \quad (12)$$

The  $C_d$  may be determined as a function of the “local” Reynolds number when no interaction between individual cylinders occurs. That is, the effect of each cylinder on the flow occurs in isolation (no sheltering or blockage). The “local” Reynolds number is then computed at point  $x$  from  $U(x)$  and  $D$  as  $Re_d = UD/\nu$ , where  $\nu$  is the kinematic viscosity. At a given local Reynolds number, the  $C_d$  for an isolated cylinder (labeled as  $C_{d-iso}$ ) can be approximated by [Cheng, 2012]:

$$C_{d-iso} = 11Re_d^{-0.75} + 0.9\Gamma_1(Re_d) + 1.2\Gamma_2(Re_d), \quad (13)$$

where

$$\Gamma_1(Re_d) = 1 - \exp\left(-\frac{1000}{Re_d}\right), \quad (14)$$

and

$$\Gamma_2(Re_d) = 1 - \exp\left[-\left(\frac{Re_d}{4500}\right)^{0.7}\right]. \quad (15)$$

A large number of experiments suggest that in dense cylindrical canopies, the assumption that each cylinder acts on the flow in isolation is not entirely valid [Poggi et al., 2004a]. Other experimental evidence also suggest that the friction factor  $f$  for vegetated surfaces varies as a function of parameters other than the local Reynolds number (i.e., other than the local bulk velocity and roughness element length scale) [Kouwen and Fathi-Moghadam, 2000; Fathi-Moghadam et al., 2011]. These deviations are commonly attributed to the type of interaction between the flow and the cylinders, which can be classified into two categories: blocking and sheltering. When the bulk Reynolds number is sufficiently small so that viscous effects cannot be ignored relative to the form drag, the viscous boundary layers forming around the cylinders along the lateral direction generate a wide slow-moving flow region with a path smaller than the spacing between cylinders. This low-velocity region results in a *higher* resistance than expected from an isolated cylinder case, so that  $C_d > C_{d-iso}$ . This effect is labeled as a “blocking effect.” Previous studies [Tanino and Nepf, 2008] verified the occurrence of the “blocking effect” showing that when  $Re_d < 1000$ ,  $C_d$  increases with (i) increasing vegetation density and (ii) decreasing  $Re_d$ . However, the opposite occurs at very high Reynolds number (i.e.,  $Re_d \gg 1000$ ). In this case, the laminar boundary attached to the solid interface is sufficiently thin relative to the rod spacing so that the “blocking effect” is entirely suppressed. Instead, the cylinders become a new source of turbulent kinetic energy (wake production) with horizontal vortices resembling von Karman streets. These von Karman streets grow in size, experiencing a form of an inverse cascade after being spawned from the cylinders. This growth is self-limiting because the interaction between these wakes and the cylinders sets a maximum size attained for the vortices. An increase in mean velocity leads to an increase in the rate at which the von Karman vortices are spawned (at frequency =  $f_{VKS}$ ) and fill the space between the cylinders. Hence, increasing the Reynolds number actually leads to a *decrease* in the drag coefficient. This leads to  $C_d < C_{d-iso}$ , an effect commonly labeled as “sheltering effect.” The sheltering effect has been shown to occur in flume experiments for a uniform rod canopy at high Reynolds number [Poggi et al., 2004b]. Viewed differently, in the case of an isolated cylinder, the local velocity relaxes to its background state at sufficiently large distance from the cylinder. The drag coefficient is dictated by the extent of the region needed for the flow to reattain this background state from its no-slip value at the cylinder-fluid interface. In the case of low  $Re_d$ , this background state is unaltered but the extended (viscous) region becomes

comparable to the separation distance between the rods, resulting in “blockage.” In the case of very high  $Re_d$ , a new background (and almost well mixed) state emerges, filling much of the space within the array of cylinders. The new background state is sustained by more frequent spawning of von Karman streets by the rods with increasing  $U$ . For the experiments here, the flow is likely to experience more frequently “blockage” instead of “sheltering” effects. There is a third effect that is entirely absent in the uniform flow case, which arises from the nonuniformity in the advective and  $dH/dx$  terms and shares some resemblance to “dispersive” stresses (i.e., stresses arising from spatial variability around the uniform flow state). Those effects can impact  $C_d$  when the flow is approximated by a locally uniform state. As shown later, such effects can lead to anomalous  $C_d$ - $Re_d$  relations that are nonmonotonic.

Cheng and Nguyen [2010] reported a monotonic decline in  $C_d$  but with an increasing vegetation-related Reynolds number ( $Re_v$ ) for canopies composed of cylinders. These experiments, presumed to represent uniform and nonuniform flow conditions, are dominated by the “blocking effect” [Ishikawa et al., 2000; James et al., 2004; Tanino and Nepf, 2008; Liu et al., 2008; Ferreira et al., 2009; Kothyari et al., 2009; Stoesser et al., 2010]. Their empirical drag coefficient for vegetation array (labeled as  $C_{d-array}$ ) fitted to a large library of experiments (the range of  $\phi_{veg}$  is 0.0022–0.35, and range of  $Re_v$  is  $50 - 6 \times 10^5$ ) is given as [Cheng and Nguyen, 2010]

$$C_{d-array} = 50(Re_v)^{-0.43} + 0.7 \left[ 1 - \exp \left( -\frac{Re_v}{15000} \right) \right], \quad (16)$$

where  $Re_v = UR_v/\nu$  is the vegetation-related Reynolds and  $R_v$  (that differs from  $R$ ) is a vegetation-related hydraulic radius given by

$$R_v = \frac{\pi}{4} \frac{1 - \phi_{veg}}{\phi_{veg}} D. \quad (17)$$

Note that  $R_v$  includes the effects of  $D$  and  $\phi_{veg}$ .

The  $C_{d-iso}$  and  $C_{d-array}$  can be used for determining  $C_d$  so as to solve for  $H(x)$  in the SVE across a range of vegetation densities and configurations trialed in the experiments (described next). The results are evaluated in terms of the ability of the parametrized SVE to reproduce the observed, steady state,  $H(x)$  along the vegetated section.

To further analyze deviations in  $C_d$  from the aforementioned predicted behavior (isolated and blocking) due to flow nonuniformity, the spatial variations in  $C_d$  can be inferred using an inversion procedure applied to the SVE so as to obtain  $C_{d-new}(x)$  from the flume data.

## 2.2. Inverting for $C_d$

The observed  $H(x)$  for various vegetation densities assembled from the flume experiments can be analyzed to obtain an empirical estimate of the spatial variations in the drag coefficient  $C_{d-new}$  as follows. Substitute equation (10) into equation (2) to obtain

$$C_{d-new} = \frac{2g(1 - \phi_{veg})}{mD} (P^* - A^*), \quad (18)$$

with a pressure component ( $P^*$ ) originating from  $\partial(p/\gamma)/\partial x$  of equation (1) given as

$$P^* = \left( -\frac{\partial H}{\partial x} \right) \frac{1}{U^2}, \quad (19)$$

and an advection component ( $A^*$ ), originating from  $\partial(\alpha_v U^2/(2g))/\partial x$  in equation (1)

$$A^* = \left( -\frac{\partial H}{\partial x} \right) \frac{1}{gH}. \quad (20)$$

Implementing this procedure raises the pragmatic question of how to estimate  $\partial H/\partial x$  from the measured  $H(x)$  that inherently contains nontrivial noise and oscillations that cannot be approximated by monochromatic waves.

### 2.3. Noise Reduction in $H(x)$ and $\partial H/\partial x$

Obtaining a reasonable estimate of  $\partial H/\partial x$  from imaged  $H(x)$  is challenging because approximations to the differential operator are sensitive to the noise level in the measured  $H(x)$  surface. Smoothing the measured  $H(x)$  to ensure that local approximations to the derivative are compatible with the global shape of the water surface can ameliorate some of this uncertainty. Optimally, the  $H(x)$  surface could be approximated by a continuous and smooth function that is both (i) analytically differentiable and (ii) can be robustly inferred from  $H(x)$  measurements without overfitting. This function must also satisfy some additional elementary constraints, including  $\partial H/\partial x < 0$  and  $\partial^2 H/\partial x^2 < 0$  as expected for gradually varied flows of the M2 type [Subramanya, 2009]. An effective mathematical function that satisfies these two constraints is:

$$\frac{\partial H}{\partial x} = \frac{c_1}{x - c_2}, \quad (21)$$

where  $c_1$  and  $c_2$  are the constants to be determined from regression analysis of  $H(x)$  upon  $x$ . The  $H(x)$  can be estimated by integrating equation (21) to yield

$$H = c_1 \ln |x - c_2| + c_3, \quad (22)$$

where  $c_3$  is an integration constant. A "robust regression" scheme using MATLAB Software (version 14, MathSoft) was used to determine  $c_1$ ,  $c_2$ , and  $c_3$  from measured  $H(x)$  for all runs (robust regression gives less weight to outliers in the inference of  $c_1$  to  $c_3$ ). As expected, the boundary conditions on the flow depth  $H(0)$ ,  $H(L) > H_{cr}$ , the vegetated section length  $L$  as well as  $\phi_{veg}$  impact the numerical values of  $c_1$ ,  $c_2$ , and  $c_3$ , where  $H_{cr}^3 = [(Q/B)^2]/g$  is the critical depth expected to occur at  $x/L > 1$  in the vicinity of the drop positioned shortly after the end of the vegetated section as discussed next.

## 3. Experiments

Flume experiments were conducted in a 10 m long,  $B = 0.3$  m wide glass flume at the State Key Laboratory of Water Resources and Hydro-power Engineering Science at Wuhan University in China. Figure 1f shows a typical side-view image of the vegetation and the water surface. The flume bed is set flat ( $S_0 = 0$ ). The vegetation was represented by plastic cylinders with each cylinder having a diameter  $D = 8$  mm and a length of  $h_v = 250$  mm. The flow rate was selected to ensure that the vegetation remained emergent for all experimental trials.

The cylinders were positioned on a 10 mm thick plastic board covered with holes to accommodate the cylinders and facilitate variation in  $\phi_{veg}$ . Although the physical set up has similarities to previous experiments [e.g., Tanino and Nepf, 2008], the cylinders here were arranged in a regular linear configuration (unlike the random arrays used in the previous studies) to ensure a locally uniform resistance. Eight vegetation densities and patch lengths, labeled Runs A to H throughout and summarized in Table 1, were undertaken with  $\phi_{veg} = 0.419, 0.291, 0.206, 0.163, 0.073, 0.041, 0.018, 0.010$ , respectively. For all the runs, a steady flow rate was set to  $Q = 0.00384 \text{ m}^3 \text{ s}^{-1}$ . Because of the drop structure after the vegetated patch, the water depth in the vicinity of the drop must traverse  $H_{cr}$  that is fixed for a specified  $Q$  and  $B$ . Hence, the degree of flow non-uniformity across the vegetation patch (and the upstream depth prior to the vegetation patch) was controlled by the vegetation patch length  $L$ , also summarized in Table 1. The combination of  $Q$  and selected  $L$  ensured that  $H_{cr} < H(x) < h_v$  for all  $\phi_{veg}$ .

When the flow attained steady state, the flow depth  $H(x)$  for each  $\phi_{veg}$  was captured by a side-view camera, illustrated here in Figure 1f for Run A. It should be noted that  $H(x)$  was measured from the upper surface of the plastic board to the flow surface. From such images,  $H(x)$  is delineated for the flow surface line for each  $\phi_{veg}$ . For reference,  $x = 0$  denotes the starting point (inlet) of the flow into the vegetation zone (normalized  $x^+ = x/L \leq 1$ ). When presenting the water level measurements, the normalized  $H^+(x) = H(x)/H_0$  where  $H_0 = H(0)$  is used to emphasize the degree of nonuniformity. The measured  $H_0$  values just upstream from the vegetation section are summarized in Table 1.

Four boards with different  $\phi_{board} = 0.419, 0.291, 0.206$ , and  $0.163$  were used to construct the  $\phi_{veg} = 0.419, 0.291, 0.206, 0.163, 0.073, 0.041, 0.018, 0.010$ . The  $\phi_{board}$  is defined as the fractional area covered by holes on the bare board, i.e.,  $\phi_{board} = m_0 \pi D^2 / 4$ , with  $m_0$  being the number of holes on the bare board per unit board area. For Runs A, B, C, and D,  $\phi_{board} = \phi_{veg}$ , i.e., all the holes were occupied by a



**Table 1.** Parameters of Each Case in the Experimental Runs<sup>a</sup>

Run	$\phi_{veg}$	$\phi_{board}$	$\phi_{hole}$	$L$ (m)	$H_0$ (m)	$c_1$	$c_2$	$c_3$
A	0.419	0.419	0	0.7125	0.2145	0.0753	0.8223	0.2280
B	0.291	0.291	0	0.6353	0.1379	0.0427	0.7241	0.1494
C	0.206	0.206	0	0.6482	0.1107	0.0312	0.7224	0.1176
D	0.163	0.163	0	0.6581	0.0984	0.0282	0.7462	0.1058
E	0.073	0.291	0.218	0.6162	0.0715	0.0192	0.7410	0.0767
F	0.041	0.163	0.122	0.6560	0.0628	0.0182	0.7818	0.0655
G	0.018	0.291	0.273	0.5251	0.0536	0.0110	1.0069	0.0528
H	0.010	0.163	0.153	0.5275	0.0466	0.0897	5.6622	−0.1087

<sup>a</sup>Note:  $\phi_{hole} = \phi_{board} - \phi_{veg} \cdot c_1$ ,  $c_2$ , and  $c_3$  are directly from the fitting of measured water surface profile.

cylinder. In Runs E and F, cylinders were embedded in alternate holes in the  $x$  and  $y$  direction of the board, while for Runs G and H, cylinders were embedded in every third hole on the board. Table 1 lists  $\phi_{board}$ ,  $\phi_{veg}$ , and  $\phi_{hole}$  (denoting the fractional area of holes on the board after embedding the cylinders) for all runs.

## 4. Results and Discussion

The results and discussion are structured as follows: section 4.1 presents a comparisons between imaged and modeled  $H(x)$  using  $C_{d-iso}$  given by equation (13) (no interaction between cylinders) and  $C_{d-array}$  given by equation (16) (interaction derived from other experiments due to blockage) for all the  $\phi_{veg}$  cases. As shown later, both  $C_d$  formulations fail to reproduce measured  $H(x)$  in regions of high flow nonuniformity (Figure 2). This failure prompted interest in how  $C_d$  empirically varies along  $x$  (related to local Reynolds number) for different  $\phi_{veg}$ . Section 4.2 shows the empirical determinations of  $H(x)$  and  $\partial H/\partial x$  needed for determining  $C_{d-new}$  empirically, with reasonable fit to the experiments. Using these fitted results to  $H(x)$ , the determination of the empirical  $C_{d-new}$  is presented in section 4.3. The empirical  $C_{d-new}$  exhibits a nonmonotonic character along with Reynolds number ( $Re_v$  or  $Re_d$ ), showing a parabolic-like pattern for each  $\phi_{veg}$  due to  $U$  variations along  $x$ . Section 4.4 explores the possible causes for such nonmonotonic character by analyzing the behavior of two terms—Pressure ( $P^*$ ) and Advection ( $A^*$ ) components—in the streamwise direction. It is shown that the interaction between  $P^*$  and  $A^*$ , arising from nonuniformity in the flow, contributes to this near-parabolic behavior. A summary formulation for  $C_d(x)$  that encodes much of the  $H(x)$  data here and may be operationally used in the SVE while accommodating the variations in  $\phi_{veg}$ ,  $Re_d$ , and  $Re_v$  is presented in section 4.5. Finally, the impacts of ground and sidewall frictions are discussed in section 4.6. The outcome of this analysis suggests that neglecting ground and sidewall frictions is reasonable for the experiments here.

### 4.1. Data-Model Comparisons

Figure 2 presents a comparison between measured normalized  $H^+ (= H(x)/H_0)$  and SVE model calculations when setting  $C_d$  to  $C_{d-iso}$  and  $C_{d-array}$  for all  $\phi_{veg}$  cases. In the SVE calculations, each vegetated section was decomposed into  $m_g = 1000$  grid points, so that  $\Delta x = L/m_g$ . Starting with the initial upstream condition set by the measurements  $H_0$ , the downstream  $H$  and  $U$  are iteratively solved between  $x = 0$  and  $x = \Delta x$  assuming  $U(x) = Q/(B_e H(x))$ . The solution at  $x = \Delta x$  serves as the upstream condition when progressing from  $x = \Delta x$  to  $x = 2\Delta x$ , and so forth until the entire vegetation section is covered or critical depth is attained. To ensure grid independence,  $m_g$  was dropped to 500 and the maximum difference in  $H$  between the two  $m_g$  solutions differed by less than 0.1%. It is evident from the comparison in Figure 2 that when  $C_d$  is set to  $C_{d-iso}$ , the SVE model calculations (green lines in Figure 2) overestimate the measured  $H(x)$  for all  $\phi_{veg}$ . The overestimation of  $H(x)$  is large in the normalized  $x^+ (= x/L)$  region experiencing the highest nonuniformity (i.e., near the outlet). When setting  $C_d$  to  $C_{d-array}$  (and hence accounting for blockage), the SVE calculations (red lines in Figure 2) underestimate the measured  $H(x)$  for higher nonuniformity, and then tends to overestimate measured  $H(x)$  for lower nonuniformity. Only for the two sparsest vegetation cases ( $\phi_{veg} < 0.02$ ), acceptable agreements were shown between the model calculations and measured  $H(x)$ . The degree of nonuniformity for the sparsest two vegetation cases is small suggesting that nonuniformity in flow causes deviations between SVE calculated and modeled  $H(x)$  in the denser vegetation conditions. This comparison demonstrates that for a nonuniform flow, the use of SVE with  $S_f$  estimated from  $C_{d-iso}$  and recent corrections

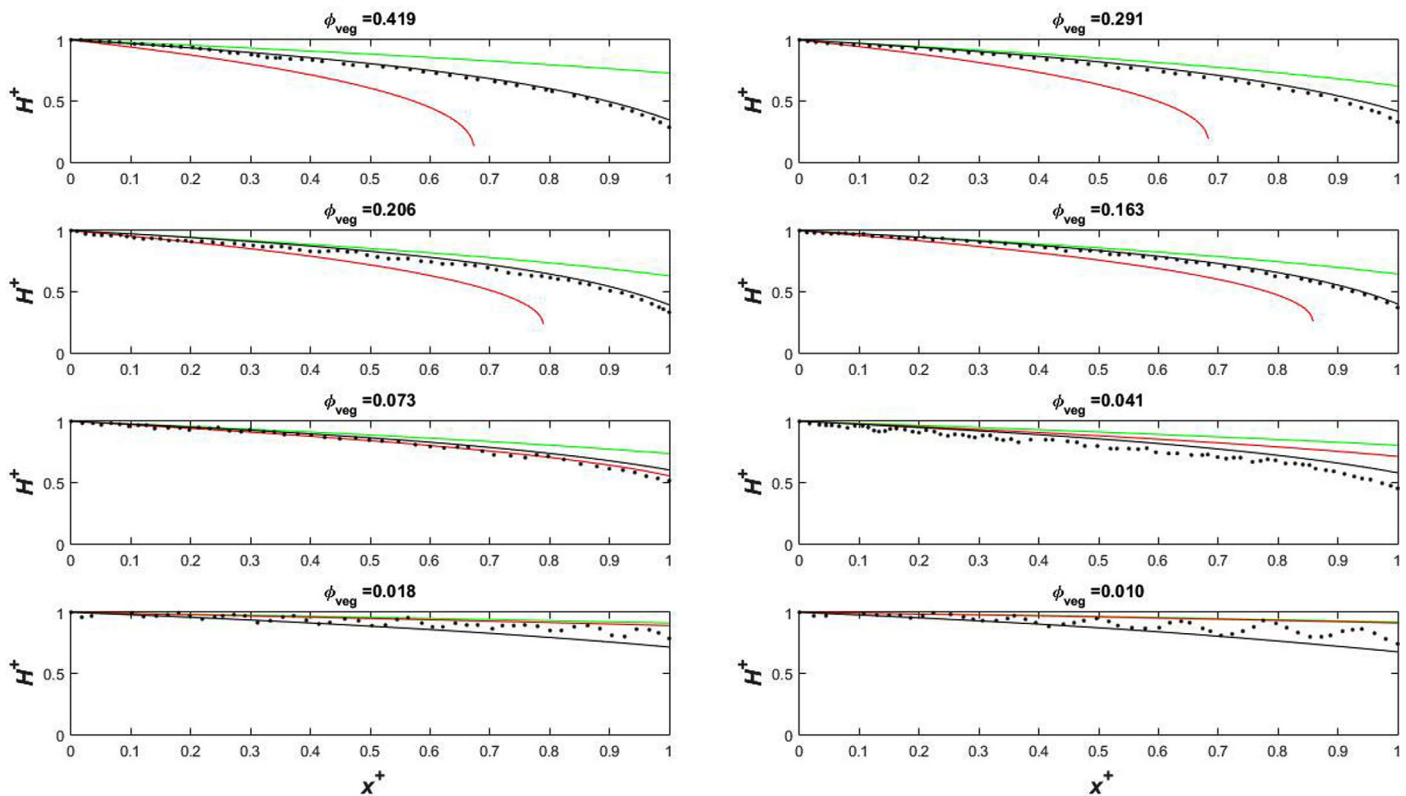


**Figure 2.** Comparison between measured and predicted normalized water level  $H^+ = H(x)/H_0$  along the normalized streamwise direction  $x^+ = x/L$  using the Saint-Venant equation for each  $\phi_{veg}$  case with different  $C_d$  approximations (different color lines). Dots indicate measured values from the side-view camera, the green lines are predictions made using  $C_{d-iso}$ , the red lines are predictions made using  $C_{d-array}$ , and the black lines are based on the newly proposed  $C_{d-new}$  model for steady nonuniform flow within cylindrical emergent vegetation.

to them (mainly due to blockage) such as those in  $C_{d-array}$  remain unsatisfactory. This lack of agreement between measurements and model calculations motivated the empirical analysis to infer the appropriate  $C_d(x)$  to be used in the SVE calculations so as to optimally recover the flume experiment measured  $H(x)$  (or their smoothed version).

#### 4.2. Empirical Determination of $H(x)$ and $\partial H/\partial x$

The outcome of the regression analysis used to approximate the measured  $H(x)$  surfaces with the function given in equation (22) is summarized in Table 1. Figures 3 and 4 demonstrate acceptable agreement between measured and fitted (i)  $H(x)$  and (ii)  $\partial H(x)/\partial x$  functions, respectively. This analysis suggested that equation (22) can be reliably used to represent the “smoothed”  $H(x)$  data for the purposes of calculating the empirical  $C_{d-new}(x)$  in equation (18) for Runs A to F. However, for Runs G and H, obvious “waviness” in the flow surface introduces additional noise in the estimated  $\partial H(x)/\partial x$ . So in the following discussion, regression parameters ( $c_1$ ,  $c_2$ , and  $c_3$ ) for Runs G and H were not considered.

#### 4.3. Inverse Computation of $C_{d-new}$

Figure 5a presents the empirical drag coefficient  $C_{d-new}$  variations with variations in  $Re_d$  (that ranges from 830 to 3530) for each  $\phi_{veg}$ , showing a nonmonotonic character. Figure 5b presents the normalized ratio of the empirical drag coefficient to the computed isolated vegetation element case  $C_{d-new}/C_{d-iso}$  for each  $\phi_{veg}$  along with  $Re_d$ . Figures 5a and 5b are similar because the computed  $C_{d-iso}$  does not change much around unity for  $Re_d$  ranging from 830 to 3530 when compared with  $C_{d-new}$ . The  $C_{d-new}/C_{d-iso}$  increases from the inlet (low  $Re_d$ ), reaching a peak value, and then decreases toward the outlets (higher  $Re_d$ ) reaching  $C_{d-new}/C_{d-iso} = 1$  when  $Re_d \approx 3000$  (this value somewhat varies for different  $\phi_{veg}$ ). The decline in  $C_{d-new}/C_{d-iso}$  with increased  $Re_d$  up to unity appears to resemble the blockage effect. From this point onward,  $C_{d-new}/C_{d-iso} < 1$  and resembles sheltering effects. Overall, the blocking effect resulted in  $C_{d-new}/C_{d-iso} \in (1, 2)$  and the sheltering effect resulted in  $C_{d-new}/C_{d-iso} \in (0.4, 1)$ .

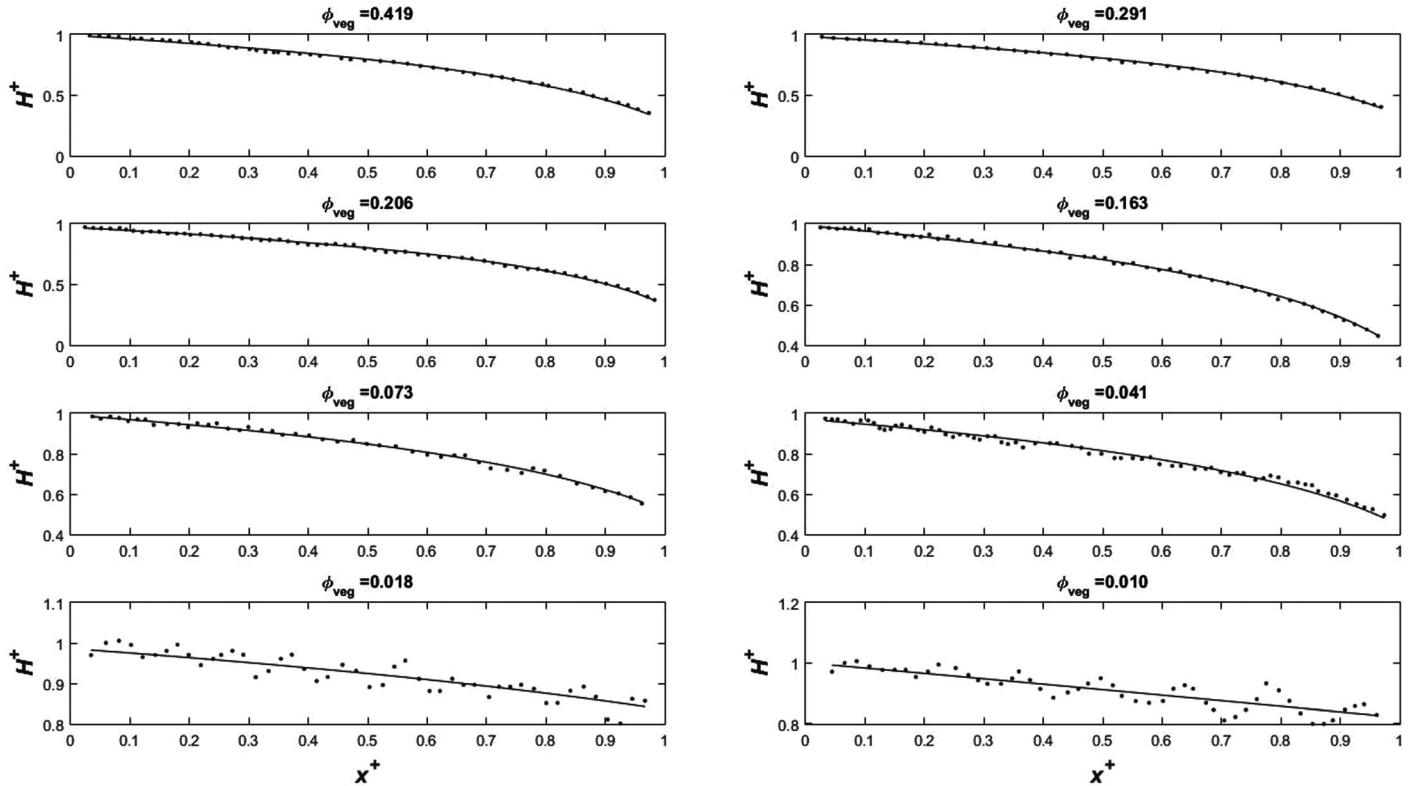


**Figure 3.** Comparison between measured and fitted normalized flow depth  $H^+ = H(x)/H_0$  along the normalized streamwise direction  $x^+ = x/L$  used to determine  $c_1$ ,  $c_2$ , and  $c_3$ . The dots indicate measurements and the line is the fitted logarithmic function. Obvious “waviness” occurs toward the outlet for  $\phi_{veg} = 0.018$  and  $0.010$ . These two runs are excluded in the empirical analysis of the  $C_d$  variation with  $Re$ .

Figure 5c shows comparison between  $C_{d-new}$  and  $C_{d-array}$  for each  $\phi_{veg}$  using the modified Reynolds number  $Re_v$  [Cheng and Nguyen, 2010] that ranges from 900 to 64,900 here. For Runs A, B, C, and D, the derived  $C_{d-new}$  appears smaller than  $C_{d-array}$  from Cheng and Nguyen [2010] (i.e., blockage underestimated relative to values obtained in the literature for uniform flow). For Runs E and F, the computed  $C_{d-new}$  crosses  $C_{d-array}$  followed by a decline after attaining a local peak. It appears that  $C_{d-new}$  is roughly bounded in magnitude between  $C_{d-iso}$  and  $C_{d-array}$  for Runs A to D and tends to cross  $C_{d-array}$  for Runs E and F, shown in Figure 5d. What is peculiar and unexpected here is the nonmonotonic behavior of  $C_d$  with increasing Reynolds number ( $Re_d$  or  $Re_v$ ), which was not observed in previous uniform flow studies. The possible origin of this anomalous nonmonotonic behavior in  $C_{d-new}$  is now further analyzed.

#### 4.4. The Nonmonotonic $C_{d-new}$ - $Re$ Relation

The ratio of the advection component ( $A^*$ ) to the pressure component ( $P^*$ ), i.e.,  $A^*/P^*$  is shown in Figure 6. When  $x/L < 0.8$ ,  $A^*$  is negligible ( $A^*/P^* < 10\%$ ) for all  $\phi_{veg} \geq 0.163$  and the flow can be reasonably treated as locally uniform. However,  $A^*/P^*$  reaches almost 60% for  $x/L > 0.8$  for  $\phi_{veg} \geq 0.163$ . For  $\phi_{veg} = 0.073$ ,  $A^*/P^*$  increases from 5% to 40%, which signifies the effect of local “advection” on  $C_d$ . The advection effect is most evident when  $\phi_{veg} = 0.041$  (sparsest case), where  $A^*/P^*$  attains a 90% value near the outlet. At this location, both advection and pressure contribute equally to  $C_d$ . To explore the interplay between these two terms further, the regression fit to  $H(x)$  are further analyzed, allowing  $C_{d-new}$  to be expressed as a function of  $Re_d$  with parameters  $c_1$ ,  $c_2$ , and  $c_3$ , expressed as

$$C_{d-new}(Re_d) = \frac{2g(1-\phi_{veg})}{mD} [P^*(Re_d) - A^*(Re_d)], \quad (23)$$

where

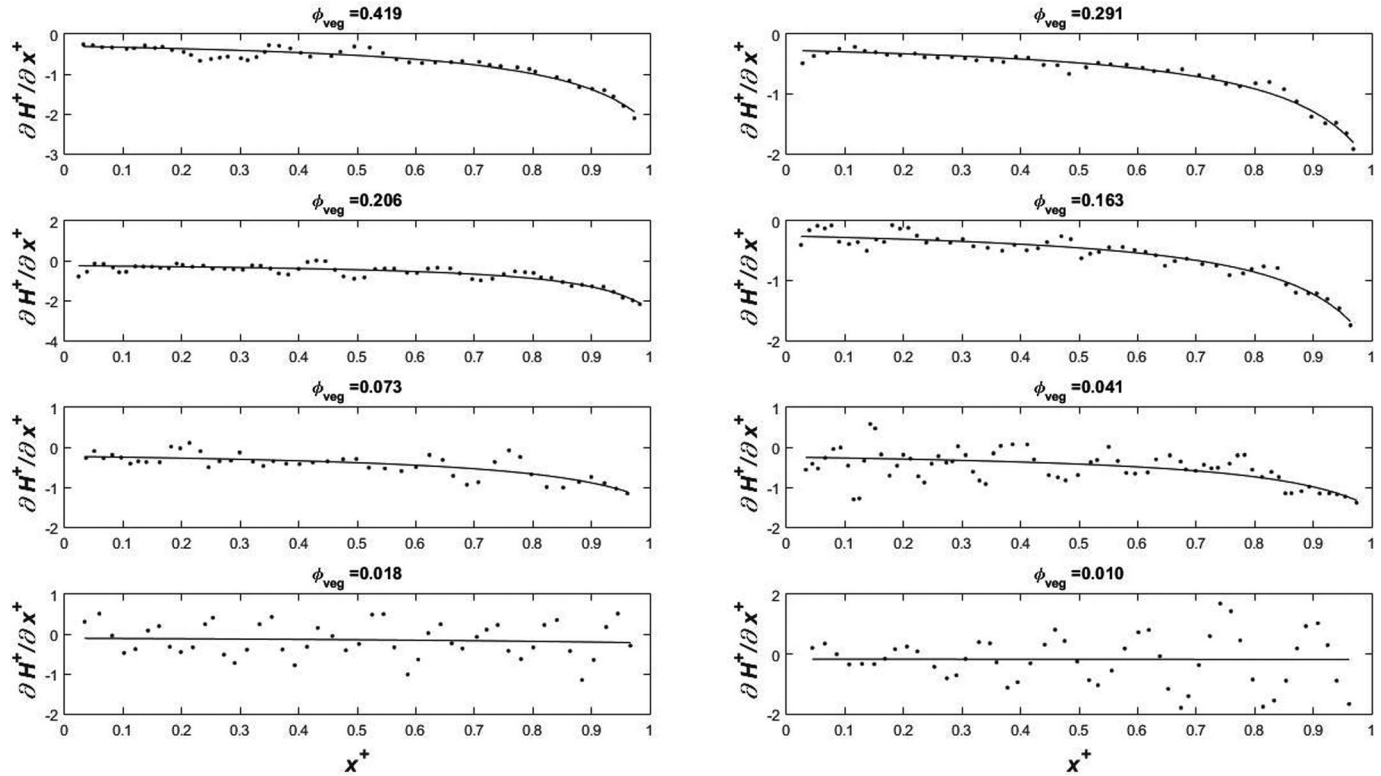


**Figure 4.** Comparison between measured and fitted normalized  $\partial H^+/\partial x^+$  along the normalized streamwise direction  $x^+ = x/L$  using the optimized  $c_1$  and  $c_2$ . The dots indicate measurements and the line is the fitted function. It is obvious that “waviness” grows toward the outlet for  $\phi_{veg}=0.018$  and  $0.010$ , introducing additional noise. These two runs are excluded in the empirical analysis of the  $C_d$  variation with  $Re$ .

$$P^*(Re_d) = (S_H D^2 \nu^{-2}) Re_d^{-2}, \quad (24)$$

and

$$A^*(Re_d) = \frac{S_H B \nu (1 - \phi_{veg})}{g Q D} Re_d, \quad (25)$$

with  $S_H$  defined as the slope of the free surface  $S_H$  (the negative value of  $\partial H/\partial x$ )

$$S_H = -\frac{\partial H}{\partial x} = c_1 \exp \left[ \frac{c_3}{c_1} - \frac{QD}{c_1 B \nu (1 - \phi_{veg})} Re_d^{-1} \right]. \quad (26)$$

The shape of  $C_d$  can be discussed in relation to  $P^*-A^*$  variations along  $x/L$ . Figure 7 shows how the parabolic-shaped  $C_d$  forms for the densest  $\phi_{veg}=0.419$  (plots a–c) and sparsest  $\phi_{veg}=0.041$  (plots d–f) cases after removing the two “wavy” surface cases. From equations (19) and (20),  $P^*-A^*=S_H[1/U^2-1/(gH)]$ . The parabolic shape can be explained by noting that the term  $[1/U^2-1/(gH)]$  decreases along  $x$  because  $1/U^2$  decreases and  $1/(gH)$  increases along the streamwise direction (Figures 7a and 7b for  $\phi_{veg}=0.419$  and Figures 7d and 7e for  $\phi_{veg}=0.041$ ) while the  $S_H=-\partial H/\partial x$  (nonuniformity) increases along the streamwise direction (Figures 7b and 7e). Clearly, the product of *increasing*  $S_H$  and *decreasing*  $[1/U^2-1/(gH)]$  with  $x$  provides a plausible explanation for the nonmonotonicity in  $C_d$ , which admits a peak when  $\partial C_d/\partial Re_d=0$  (Figures 7c and 7f). It is interesting to note here that  $S_H$  and  $P^*-A^*$  are constants in  $x$  for uniform flows and thus the nonmonotonous behavior of  $C_d$  is associated with the flow nonuniformity. A summary model of the data that encodes this behavior is now presented.

#### 4.5. A Summary Model for $C_{d-new}$

To summarize the above results as a  $C_d$  model, a  $C_{d-new}$  in equation (23) is discussed here and is based on  $c_1$ ,  $c_2$ , and  $c_3$  as a function of the main “external” variable (i.e.,  $\phi_{veg}$ ) in this experiment (given the constant  $Q$ ).

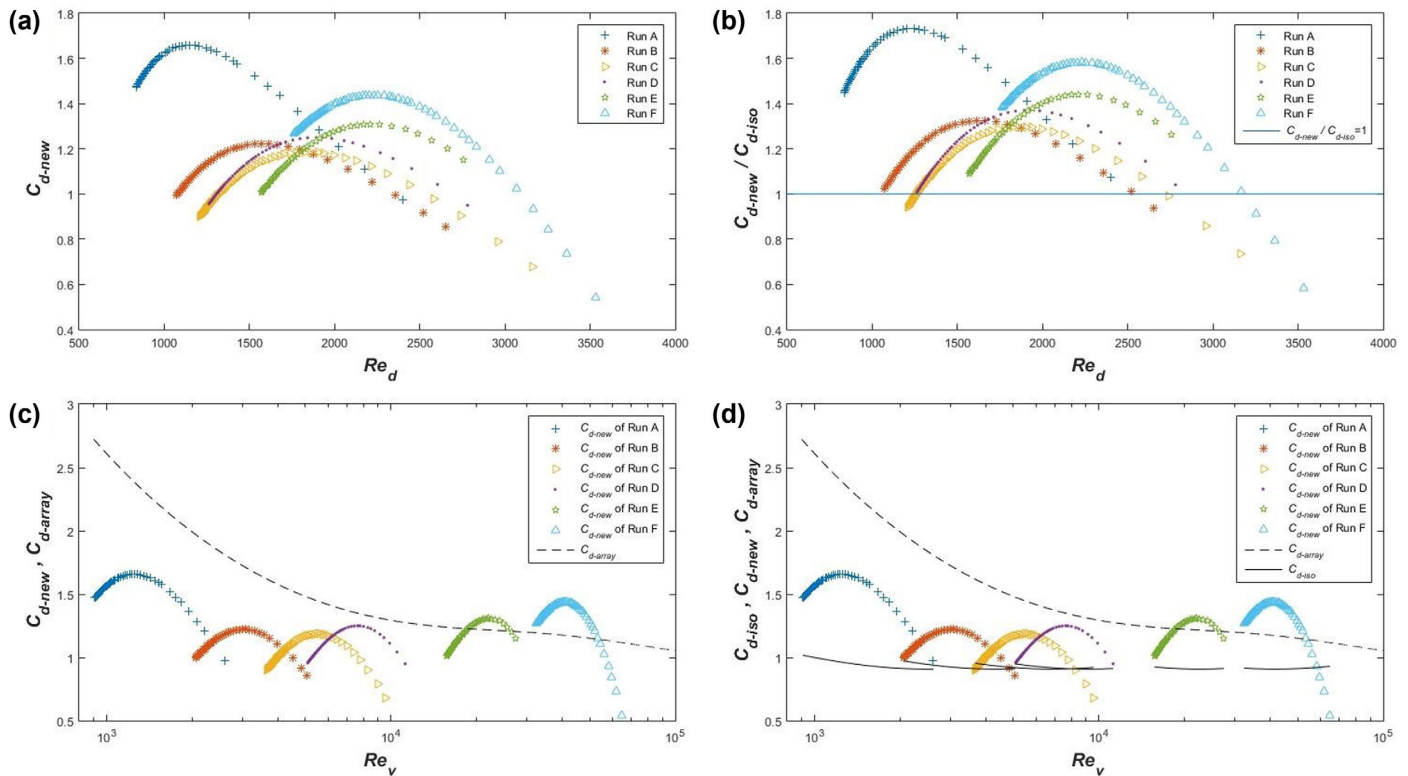


**Figure 5.** (a) Empirical  $C_{d-new}$  using data from the flume experiments along with  $Re_d = UD/\nu$ . (b) Normalized drag coefficient  $C_{d-new}/C_{d-iso}$  using data from the flume experiments along with  $Re_d = UD/\nu$ . (c) Comparison between  $C_{d-new}$  and  $C_{d-array}$  along with  $Re_v = UR_v/\nu$ . (d) Comparison among  $C_{d-iso}$ ,  $C_{d-new}$ , and  $C_{d-array}$  along with  $Re_v = UR_v/\nu$ .

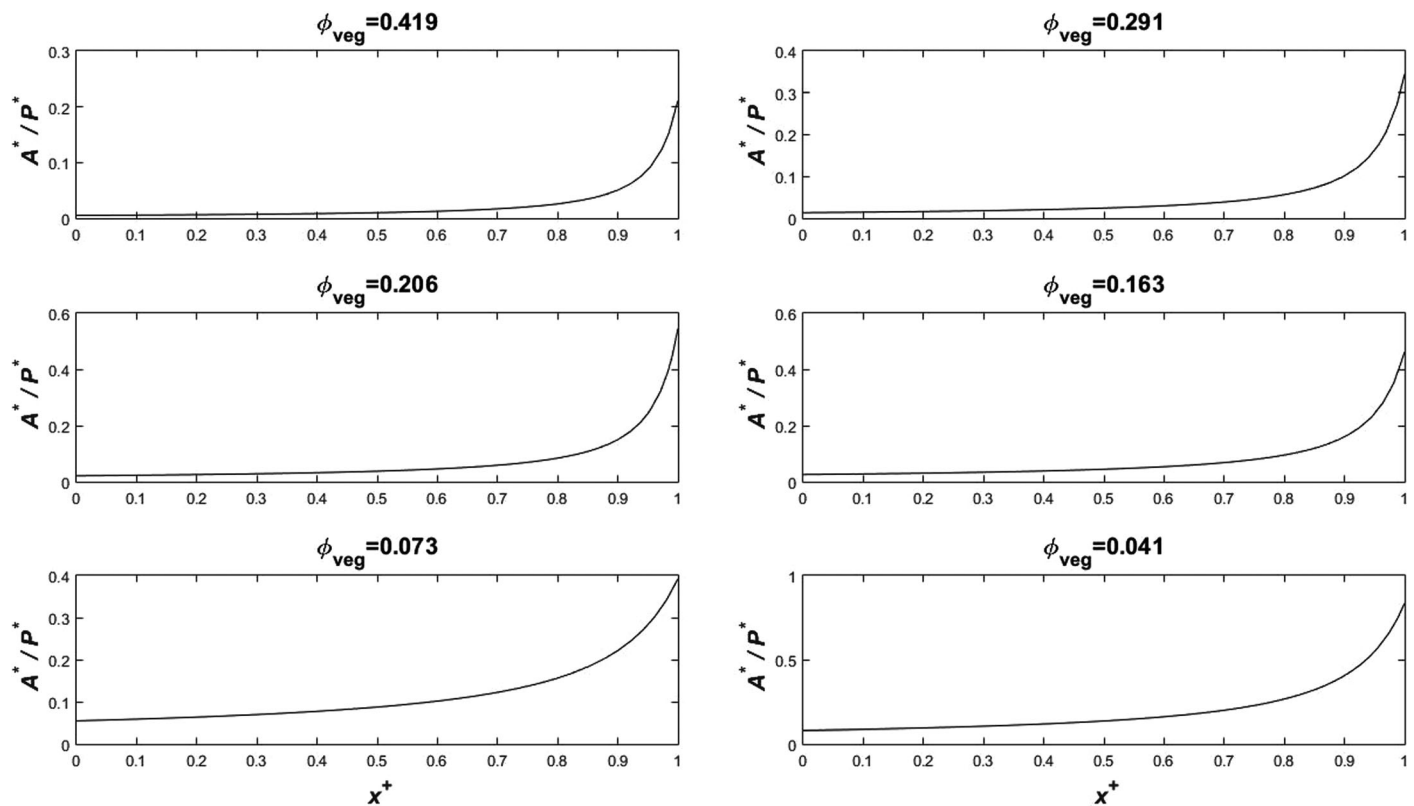


**Figure 6.** Comparison ( $A^*/P^*$ ) between the advection ( $A^*$ ) to pressure ( $P^*$ ) components for each  $\phi_{veg}$  case along the normalized streamwise direction  $x^+ = x/L$ .



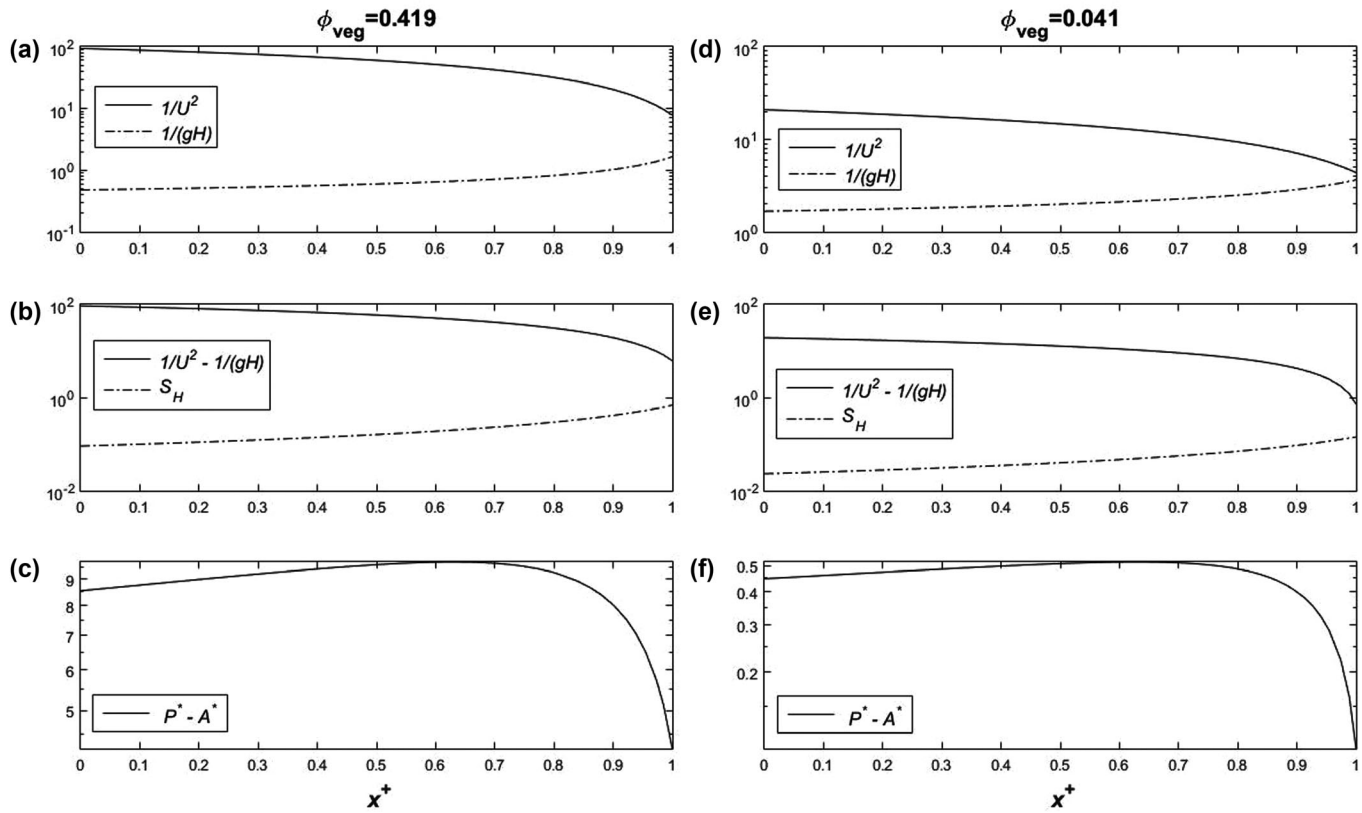


**Figure 7.** Analysis of parabolic-shaped  $C_d$  for the (left) densest case  $\phi_{veg}=0.419$  and (right) sparsest case  $\phi_{veg}=0.041$ . The individual terms governing  $P^*-A^*$  (panels c and f) are shown in panels (a)–(b) for the densest case, and (d)–(e) for the sparsest case.

Naturally,  $c_1$ ,  $c_2$  and  $c_3$  are dependent on the water depth boundary conditions  $H_0$  and  $H_{cr}$  at  $x/L > 1$  as well as  $L$ . As noted earlier, these boundary conditions provide constraints on the relation between  $c_1$  to  $c_3$  and  $Q$ ,  $H_0$ , and  $L$ . To illustrate, note that at  $x/L=0$ ,  $H(0)=H_0$  resulting in  $c_3=H_0-c_1\ln|c_2|$ . Also, for  $x/L > 1$ ,  $H(L) \geq H_{cr}$  so that  $L/c_2 \approx 1 - \exp[(H_{cr}-H_0)/c_1] < 1$ , where  $H_{cr}$  is uniquely determined by  $Q/B$ . Hence, various flow rates, upstream water depth, and vegetation patch length predictably impact  $c_1$  to  $c_3$ , but the focus here is on  $\phi_{veg}$ . Figure 8 (left) shows the optimized  $c_1$  for Runs A to F as a function of  $\phi_{veg}$ . The  $c_1$  is reasonably approximated by  $c_1 \approx 0.323\phi_{veg}^2 + 0.018$ . When  $x=0$  (inlet conditions), the water surface gradient can be used to determine  $c_1/c_2$ . Figure 8 (right) shows that  $c_1/c_2$  for Runs A to F also increase with increasing  $\phi_{veg}$  at a rate given by  $c_1/c_2 \approx 0.258\phi_{veg}^{3/2} + 0.020$ . Note when  $\phi_{veg}=0$ , the constant terms signify ground effects, which are not negligible in the absence of vegetation.

To explore the nonmonotonic  $C_d-Re$  relation on modeled  $H(x)$ , the  $c_1$  to  $c_3$  only derived from  $\phi_{veg}$  are now used to determined  $C_{d-new}$  that is then inserted into the SVE equation to solve for  $H(x)$ . Not surprisingly, acceptable agreement between measured and modeled  $H(x)$  is noted in Figure 2. This acceptable agreement supports the locally uniform flow approximation to the  $S_f$  closure in SVE despite the significance in  $A^*/P^*$  over certain regions of the flow domain. It should be noted that the empirical expressions for  $c_1$ ,  $c_2$ , and  $c_3$  were determined for  $Q = 0.00384 \text{ m}^3/\text{s}$  and further investigation is needed to assess whether parameter  $c_1$  differs across different flow rates (parameters  $c_2$  and  $c_3$  are constrained by  $Q$ ,  $H_0$ , and  $L$  once  $c_1$  is determined). As an independent test to the aforementioned  $C_{d-new}$  model (equation (23)) using a different configuration, Run E was repeated but with a staggered configuration (hereafter this additional run is labeled as Run E1). The flow rate was set to  $Q = 0.00384 \text{ m}^3/\text{s}$  and the vegetation density is the same as Run E. Figure 9 shows reasonable agreement between measured and modeled  $H(x)$  for this staggered configuration case when adopting the previously derived empirical  $c_1$ ,  $c_2$ , and  $c_3$  in the model calculations suggesting that the model results are insensitive to the precise vegetation arrangements. A sensitivity analysis was also

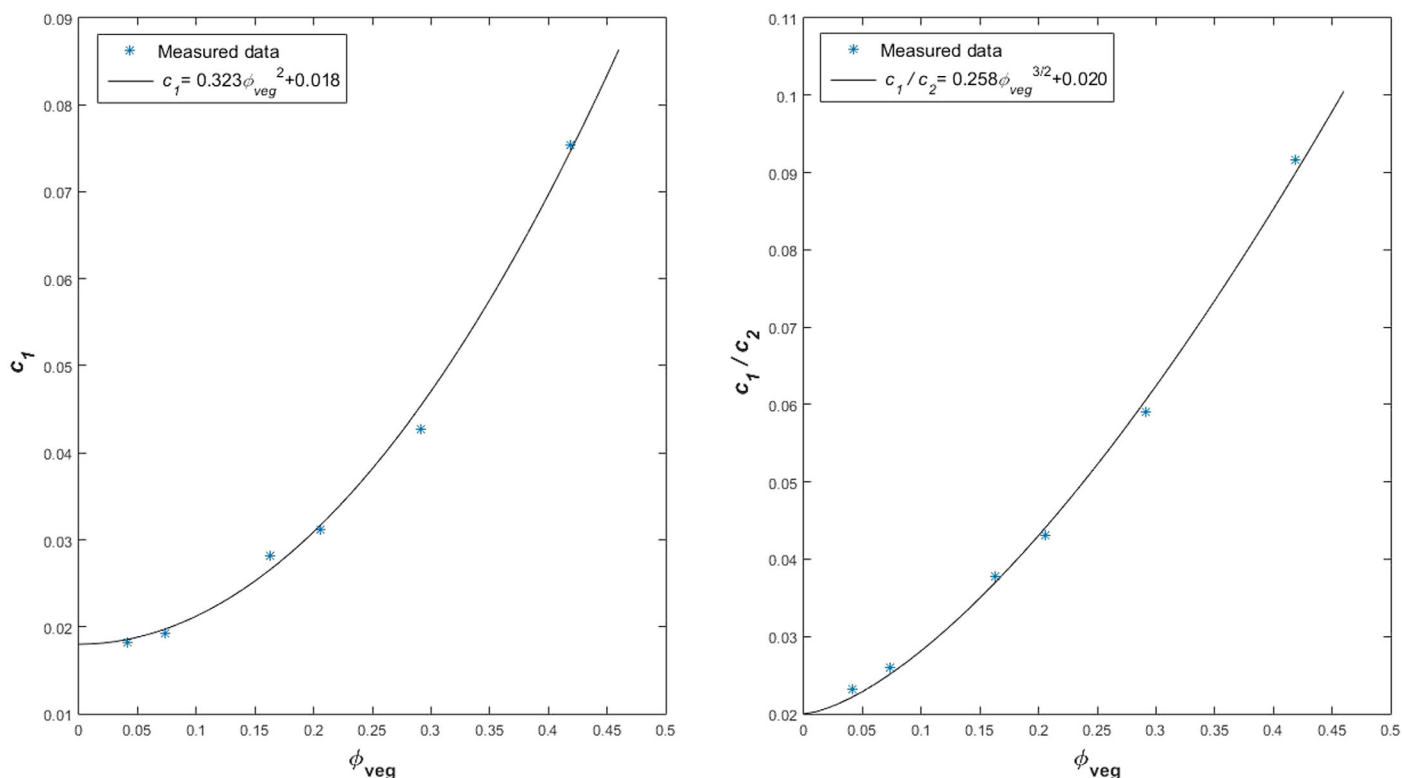


**Figure 8.** Regressing (left)  $c_1$  upon  $\phi_{veg}$ , and (right)  $c_1/c_2$  upon  $\phi_{veg}$  using the flume experiments.

conducted on  $c_1$  and  $c_2$  by varying them independently by 10% and 20% for the sparsest and densest cases with  $c_3 = H_0 - c_1 \ln |c_2|$ . The nonmonotonic  $C_d-Re$  pattern still persisted despite these variations suggesting that such pattern is not an artifact of the function used to fit  $H(x)$ .

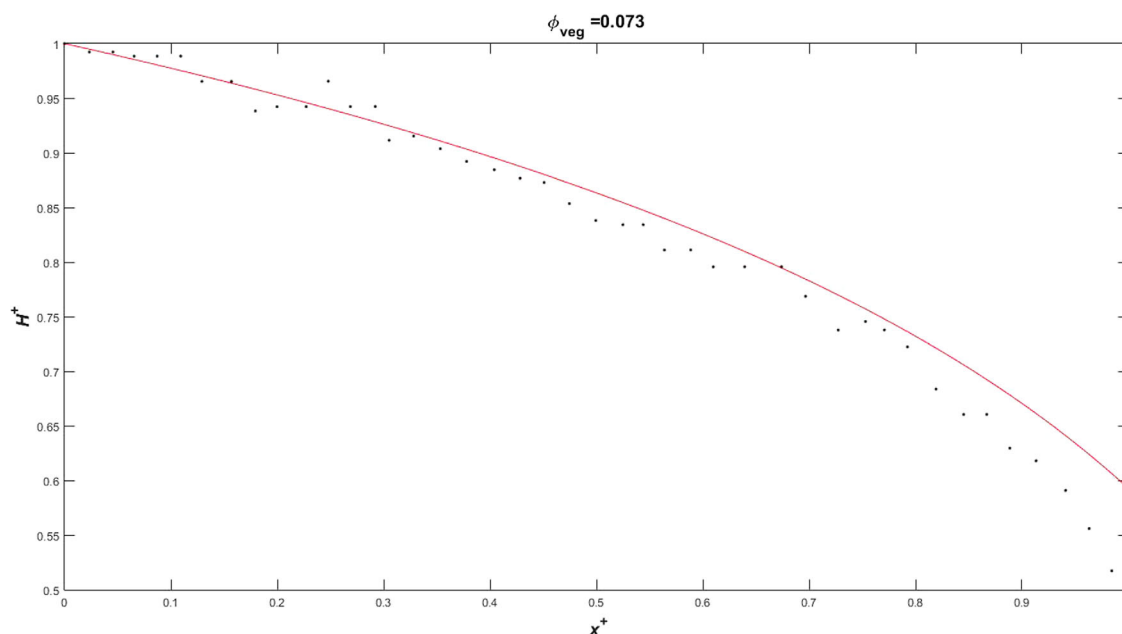


**Figure 9.** Verification of the derived model on a staggered configuration case.

#### 4.6. Impact of Ground and Sidewall Friction

Recall from the force balance equation (7), the vegetation drag term  $BF_D$  was compared against the ground friction term  $B(1 - \phi_{veg})\tau_{ground}$ , which is given as

$$\frac{B(1 - \phi_{veg})\tau_{ground}}{BF_D} = \frac{(1/\phi_{veg} - 1)\pi D f_{ground}}{16 C_d H}. \quad (27)$$

Ground friction is expected to be negligible when considering the dense vegetation cases. However, to test whether the impact of ground friction can also be neglected for the sparsest canopy case, additional experiments were conducted. Here the sparsest case, Run F, was selected for illustration. For this run, the  $\phi_{veg} = 0.041$ , the averaged  $H = 0.05$  m, and the averaged  $C_d = 1.31$ . The  $f_{ground}$  was estimated in the range of 0.01–0.1 from a Moody chart assuming the roughness height  $k_s = 0.0025$  mm for plastic boards is representative of the board material. Even if  $f_{ground} = 0.1$  is taken as a maximum roughness, the ratio of ground friction term to vegetation term (equation (27)) gives 5.6%, which provides convincing evidence for neglecting ground friction relative to vegetation for all eight runs. Similarly, vegetation drag term  $BF_D$  can be compared with the sidewall friction term  $2H\tau_{wall}$  as

$$\frac{2H\tau_{wall}}{BF_D} = \frac{\pi D f_{wall}}{8 \phi_{veg} C_d B}, \quad (28)$$

and the sparsest case, Run F, is used as illustration. Even when the extreme roughness condition  $f_{wall} = 0.1$  is used in equation (28), the ratio of sidewall friction term to vegetation drag term gives 1.9%, which also confirms the assumption that neglecting the sidewall friction is reasonable for all runs.

## 5. Conclusion

Following an intense rainfall event, there is ample evidence that water subsidy from crusted bare soil to vegetated sites is partly responsible for the maintenance of vegetation in arid and semiarid regions. This lateral subsidy tends to be most significant on flat ground where the driving gradient for flow is the gradient in the free water surface. Reasonable predictions about the volume and extent of the redistribution of water into vegetated patches are required and operationally employ the SVE subject to closure approximations. The determination of an appropriate closure model to use for flat vegetated surfaces continues to be one of the main challenges to such operational models. The flume experiments analyzed here explore a subset of these challenges with their focus on the effects of flow nonuniformity and vegetation density. They demonstrate that interaction between cylinders (sheltering, blockage, and flow nonuniformity) can significantly impact the effective friction factor or Manning roughness values used to close to the SVE. Prior calculations either assume a constant  $n$  for the vegetation section or consider an expression linking  $H$  to  $n$  as derived for uniform flow canopies. For the latter scheme with a given  $\phi_{veg}$ , the nonuniformity of flow surface leads to a monotonic  $n$  (or  $f$ ) variation along the streamwise direction. Here the nonuniformity in the flow is shown to be the leading cause for the nonmonotonic variation in  $C_d$  and its associated effects on roughness measures with increasing Reynolds number (and position).

## References

- Abrahams, A., A. Parsons, and S.-H. Luk (1986), Resistance to overland flow on desert hillslopes, *J. Hydrol.*, **88**(3), 343–363.
- Ajayi, A. E., N. van de Giesen, and P. Vlek (2008), A numerical model for simulating hortonian overland flow on tropical hillslopes with vegetation elements, *Hydrol. Processes*, **22**(8), 1107–1118, doi:10.1002/hyp.6665.
- Assouline, S., S. E. Thompson, L. Chen, T. Svoray, S. Sela, and G. G. Katul (2015), The dual role of soil crusts in desertification, *J. Geophys. Res. Biogeosci.*, **120**, 2108–2119, doi:10.1002/2015JG003185.
- Banerjee, T., M. Muste, and G. Katul (2015), Flume experiments on wind induced flow in static water bodies in the presence of protruding vegetation, *Adv. Water Resour.*, **76**, 11–28.
- Bromley, J., J. Brouwer, A. Barker, S. Gaze, and C. Valentine (1997), The role of surface water redistribution in an area of patterned vegetation in a semi-arid environment, south-west niger, *J. Hydrol.*, **198**(1–4), 1–29.
- Carollo, F. G., V. Ferro, and D. Termini (2005), Flow resistance law in channels with flexible submerged vegetation, *J. Hydraul. Eng.*, **131**(7), 554–564.
- Chen, L., S. Sela, T. Svoray, and S. Assouline (2013), The role of soil-surface sealing, microtopography, and vegetation patches in rainfall-runoff processes in semiarid areas, *Water Resour. Res.*, **49**, 5585–5599, doi:10.1002/wrcr.20360.
- Cheng, N.-S. (2012), Calculation of drag coefficient for arrays of emergent circular cylinders with pseudofluid model, *J. Hydraul. Eng.*, **139**(6), 602–611.

#### Acknowledgments

The authors thank Wu-Gang Zhou, Feng-Peng Bai, Meng Gao, and Cheng-Guang Li for their assistance with the flume experiments. Wen-Xin Huai and Wei-Jie Wang were supported by the National Natural Science Foundation of China (11372232 and 51479007). Wei-Jie Wang is also grateful to the China Scholarship Council for the financial support during a 14 month study at Duke University. G. Katul acknowledges support from the National Science Foundation (NSF-EAR-1344703 and NSF-CBET-103347), the U.S. Department of Energy (DOE) through the office of Biological and Environmental Research (BER) Terrestrial Ecosystem Science (TES) Program (DE-SC0006967 and DE-SC0011461). The raw data from the experiments are featured in Table 1 and Figures 2 and 9.

- Cheng, N.-S., and H. T. Nguyen (2010), Hydraulic radius for evaluating resistance induced by simulated emergent vegetation in open-channel flows, *J. Hydraul. Eng.*, 137(9), 995–1004.
- Dijkstra, J., and R. Uittenbogaard (2010), Modeling the interaction between flow and highly flexible aquatic vegetation, *Water Resour. Res.*, 46, W12547, doi:10.1029/2010WR009246.
- Dunkerley, D. (2002), Infiltration rates and soil moisture in a groved mulga community near Alice Springs, arid central Australia: Evidence for complex internal rainwater redistribution in a runoff-runon landscape, *J. Arid Environ.*, 51(2), 199–219.
- Fathi-Moghadam, M., K. Drikvandi, B. Lashkarara, and K. Hammadi (2011), Determination of friction factor for rivers with non-submerged vegetation in banks and floodplains, *Sci. Res. Essays*, 6(22), 4714–4719.
- Ferreira, R. M., A. M. Ricardo, and M. J. Franca (2009), Discussion of laboratory investigation of mean drag in a random array of rigid, emergent cylinders by Yukie Tanino and Heidi M. Nepf, *J. Hydraul. Eng.*, 135(8), 690–693.
- Foti, R., and J. A. Ramírez (2013), A mechanistic description of the formation and evolution of vegetation patterns, *Hydrol. Earth Syst. Sci.*, 17(1), 63–84, doi:10.5194/hess-17-63-2013.
- Galle, S., M. Ehrmann, and C. Peugeot (1999), Water balance in a banded vegetation pattern: A case study of tiger bush in western Niger, *Catena*, 37(1), 197–216.
- Ghisalberti, M., and H. Nepf (2004), The limited growth of vegetated shear layers, *Water Resour. Res.*, 40, W07502, doi:10.1029/2003WR002776.
- Green, J. C. (2005), Modelling flow resistance in vegetated streams: Review and development of new theory, *Hydrol. Processes*, 19(6), 1245–1259.
- Holden, J., M. J. Kirkby, S. N. Lane, D. G. Milledge, C. J. Brookes, V. Holden, and A. T. McDonald (2008), Overland flow velocity and roughness properties in peatlands, *Water Resour. Res.*, 44, W06415, doi:10.1029/2007WR006052.
- Huai, W.-X., Y.-H. Zeng, Z.-G. Xu, and Z.-H. Yang (2009), Three-layer model for vertical velocity distribution in open channel flow with submerged rigid vegetation, *Adv. Water Resour.*, 32(4), 487–492.
- Huai, W.-X., W.-J. Wang, and Y.-H. Zeng (2013), Two-layer model for open channel flow with submerged flexible vegetation, *J. Hydraul. Res.*, 51(6), 708–718.
- Huai, W.-X., W.-J. Wang, Y. Hu, Y.-H. Zeng, and Z.-H. Yang (2014), Analytical model of the mean velocity distribution in an open channel with double-layered rigid vegetation, *Adv. Water Resour.*, 69, 106–113.
- Huthoff, F., D. Augustijn, and S. J. Hulscher (2007), Analytical solution of the depth-averaged flow velocity in case of submerged rigid cylindrical vegetation, *Water Resour. Res.*, 43, W06413, doi:10.1029/2006WR005625.
- Ishikawa, Y., K. Mizuhara, and S. Ashida (2000), Effect of density of trees on drag exerted on trees in river channels, *J. For. Res.*, 5(4), 271–279.
- James, C., A. Birkhead, A. Jordanova, and J. Osullivan (2004), Flow resistance of emergent vegetation, *J. Hydraul. Res.*, 42(4), 390–398.
- Järvelä, J. (2002), Flow resistance of flexible and stiff vegetation: A flume study with natural plants, *J. Hydrol.*, 269(1), 44–54.
- Katul, G. G., D. Poggi, and L. Ridolfi (2011), A flow resistance model for assessing the impact of vegetation on flood routing mechanics, *Water Resour. Res.*, 47, W08533, doi:10.1029/2010WR010278.
- Kefi, S., M. Rietkerk, and G. G. Katul (2008), Vegetation pattern shift as a result of rising atmospheric CO<sub>2</sub> in arid ecosystems, *Theor. Popul. Biol.*, 74(4), 332–344.
- Kim, J., V. Y. Ivanov, and N. D. Katopodes (2012), Hydraulic resistance to overland flow on surfaces with partially submerged vegetation, *Water Resour. Res.*, 48, W10540, doi:10.1029/2012WR012047.
- Kletter, A., J. Von Hardenberg, E. Meron, and A. Provenzale (2009), Patterned vegetation and rainfall intermittency, *J. Theor. Biol.*, 256(4), 574–583.
- Konings, A. G., S. C. Dekker, M. Rietkerk, and G. G. Katul (2011), Drought sensitivity of patterned vegetation determined by rainfall-land surface feedbacks, *J. Geophys. Res.*, 116, G04008, doi:10.1029/2011JG001748.
- Konings, A. G., G. G. Katul, and S. E. Thompson (2012), A phenomenological model for the flow resistance over submerged vegetation, *Water Resour. Res.*, 48, W02522, doi:10.1029/2011WR011000.
- Kothyari, U. C., K. Hayashi, and H. Hashimoto (2009), Drag coefficient of unsubmerged rigid vegetation stems in open channel flows, *J. Hydraul. Res.*, 47(6), 691–699.
- Kouwen, N., and M. Fathi-Moghadam (2000), Friction factors for coniferous trees along rivers, *J. Hydraul. Eng.*, 126(10), 732–740.
- Kubrak, E., J. Kubrak, and P. Rowiński (2008), Vertical velocity distributions through and above submerged, flexible vegetation, *Hydrol. Sci. J.*, 53(4), 905–920.
- Lawrence, D. (2000), Hydraulic resistance in overland flow during partial and marginal surface inundation: Experimental observations and modeling, *Water Resour. Res.*, 36, 2381–2393.
- Liu, D., P. Diplas, J. Fairbanks, and C. Hodges (2008), An experimental study of flow through rigid vegetation, *J. Geophys. Res.*, 113, F04015, doi:10.1029/2008JF001042.
- Luhar, M., J. Rominger, and H. Nepf (2008), Interaction between flow, transport and vegetation spatial structure, *Environ. Fluid Mech.*, 8(5–6), 423–439.
- Nepf, H., and M. Ghisalberti (2008), Flow and transport in channels with submerged vegetation, *Acta Geophys.*, 56(3), 753–777.
- Nepf, H. M. (2012), Flow and transport in regions with aquatic vegetation, *Annu. Rev. Fluid Mech.*, 44, 123–142.
- Nikora, V., S. Larned, N. Nikora, K. Debnath, G. Cooper, and M. Reid (2008), Hydraulic resistance due to aquatic vegetation in small streams: Field study, *J. Hydraul. Eng.*, 134(9), 1326–1332.
- Nobel, P. S. (1980), Water vapor conductance and CO<sub>2</sub> uptake for leaves of a C<sub>4</sub> desert grass, *Hilaria rigida*, *Ecology*, 61, 252–258.
- Okamoto, T.-A., and I. Nezu (2013), Spatial evolution of coherent motions in finite-length vegetation patch flow, *Environ. Fluid Mech.*, 13(5), 417–434.
- Poggi, D., G. Katul, and J. Albertson (2004a), Momentum transfer and turbulent kinetic energy budgets within a dense model canopy, *Boundary Layer Meteorol.*, 111(3), 589–614.
- Poggi, D., A. Porporato, L. Ridolfi, J. Albertson, and G. Katul (2004b), The effect of vegetation density on canopy sub-layer turbulence, *Boundary Layer Meteorol.*, 111(3), 565–587.
- Poggi, D., C. Krug, and G. G. Katul (2009), Hydraulic resistance of submerged rigid vegetation derived from first-order closure models, *Water Resour. Res.*, 45, W10442, doi:10.1029/2008WR007373.
- Rietkerk, M., M. C. Boerlijst, F. van Langevelde, R. HilleRisLambers, J. van de Koppel, L. Kumar, H. H. Prins, and A. M. de Roos (2002), Self-organization of vegetation in arid ecosystems, *Am. Nat.*, 160(4), 524–530.
- Roche, N., J.-F. Daian, and D. Lawrence (2007), Hydraulic modeling of runoff over a rough surface under partial inundation, *Water Resour. Res.*, 43, W08410, doi:10.1029/2006WR005484.

- Roth-Nebelsick, A., M. Ebner, T. Miranda, V. Gottschalk, D. Voigt, S. Gorb, T. Stegmaier, J. Sarsour, M. Linke, and W. Konrad (2012), Leaf surface structures enable the endemic Namib desert grass *Stipagrostis sabulicola* to irrigate itself with fog water, *J. R. Soc. Interface*, *9*, 1965–1974, doi:10.1098/rsif.2011.0847.
- Siniscalchi, F., V. I. Nikora, and J. Aberle (2012), Plant patch hydrodynamics in streams: Mean flow, turbulence, and drag forces, *Water Resour. Res.*, *48*, W01513, doi:10.1029/2011WR011050.
- Smith, R., et al. (1995), KINEROS-a kinematic runoff and erosion model, in *Computer Models of Watershed Hydrology*, Chapter 20, edited by V. P. Singh, pp. 697–732, Water Resources Publications, Littleton, Colo.
- Stoesser, T., S. Kim, and P. Diplas (2010), Turbulent flow through idealized emergent vegetation, *J. Hydraul. Eng.*, *136*(12), 1003–1017.
- Subramanya, K. (2009), *Flow in Open Channels*, Tata McGraw-Hill Publishing Company Limited, New Delhi, India.
- Tanino, Y., and H. M. Nepf (2008), Laboratory investigation of mean drag in a random array of rigid, emergent cylinders, *J. Hydraul. Eng.*, *134*(1), 34–41.
- Thompson, S., G. Katul, and S. M. McMahon (2008), Role of biomass spread in vegetation pattern formation within arid ecosystems, *Water Resour. Res.*, *44*, W10421, doi:10.1029/2008WR006916.
- Thompson, S., C. Harman, P. Heine, and G. Katul (2010), Vegetation-infiltration relationships across climatic and soil type gradients, *J. Geophys. Res.*, *115*, G02023, doi:10.1029/2009JG001134.
- Thompson, S., G. Katul, A. Konings, and L. Ridolfi (2011), Unsteady overland flow on flat surfaces induced by spatial permeability contrasts, *Adv. Water Resour.*, *34*(8), 1049–1058.
- Valentin, C., and J.-M. d'Herbès (1999), Niger tiger bush as a natural water harvesting system, *Catena*, *37*(1), 231–256.
- Velasco, D., A. Bateman, and V. Medina (2008), A new integrated, hydro-mechanical model applied to flexible vegetation in riverbeds, *J. Hydraul. Res.*, *46*(5), 579–597.
- Wang, W.-J., W.-X. Huai, Y.-H. Zeng, and J.-F. Zhou (2015), Analytical solution of velocity distribution for flow through submerged large deflection flexible vegetation, *Appl. Math. Mech.*, *36*(1), 107–120.
- Wasson, R., and P. Nanninga (1986), Estimating wind transport of sand on vegetated surfaces, *Earth Surf. Processes Landforms*, *11*(5), 505–514.
- Woolhiser, D. A., and J. A. Liggett (1967), Unsteady, one-dimensional flow over a plane—The rising hydrograph, *Water Resour. Res.*, *3*, 753–771.
- Yang, W., and S.-U. Choi (2009), Impact of stem flexibility on mean flow and turbulence structure in depth-limited open channel flows with submerged vegetation, *J. Hydraul. Res.*, *47*(4), 445–454.